

## Supporting Information

### Chemical Prelithiation of Al as an Ambient Air Compatible and Polysulfide Resistant Anode for Li-ion/S Batteries

Yongmin Huang,<sup>a</sup> Chang Liu,<sup>a</sup> Fengyuan Wei,<sup>a</sup> Gongwei Wang,<sup>a\*</sup> Li Xiao,<sup>a</sup> Juntao Lu,<sup>a</sup> and Lin Zhuang<sup>a,b</sup>

<sup>a</sup>College of Chemistry and Molecular Sciences, Hubei Key Lab of Electrochemical Power Sources, Wuhan University, Wuhan 430072, China. E-mail: gwwang@whu.edu.cn

<sup>b</sup>Institute for Advanced Studies, Wuhan University, Wuhan 430072, China.

#### 1. Material and methods

##### 1.1. Preparation of Li-DiMF/THF solution

The chemical prelithiation reagent (1 M Li-DiMF/THF) was prepared by the direct reaction of lithium metal and 9,9-Dimethylfluorene (DiMF) in anhydrous tetrahydrofuran (THF) solution. Typically, 0.97 g of DiMF (98%, Aladdin Chemistry) was dissolved in 5 ml of THF ( $\geq 99.9\%$ , Aladdin Chemistry). Then a piece of lithium metal (ca. 0.04 g) was added into the solution for 30 min reaction.

##### 1.2. Anode preparation

A commercial Al foil (99.9%, 100  $\mu\text{m}$  thick, Shanghai Yuanbao Metal Material) was used as both the anode and current collector. The Al foil was polished with a metallographic sandpaper (1200 mesh) to remove the thick alumina ( $\text{Al}_2\text{O}_3$ ) layer. The free-standing LiAl anode (*c*-LiAl) was obtained by immersing the single-side polished Al foil in prelithiation reagent (1 M Li-DiMF/THF) for 5 min treatment unless otherwise specified, followed by washing with anhydrous THF and vacuum drying at room temperature.

For comparison, another type of free-standing LiAl anode was also prepared via electrochemical prelithiation (*e*-LiAl) using a half cell configuration. The working electrode was also a single-side polished Al foil and the counter electrode was a lithium metal foil (600  $\mu\text{m}$ ). The separator was Celgard 2325 membrane and the electrolyte was 1 M LiTFSI in DME/DOL (1:1, v/v) with 0.4 M  $\text{LiNO}_3$  additive. The cell was lithiated to 0.8 mAh  $\text{cm}^{-2}$  and delithiated to 2 V for 5 cycles at a current density of 9.6 mA  $\text{cm}^{-2}$  (Fig. S8a). Each electrochemical lithiation step was 5 min. A lithium metal anode (*e*-Li/Cu) was prepared by a similar method with *e*-LiAl except using a Cu foil as the working electrode and a current density of 0.5 mA  $\text{cm}^{-2}$  (Fig. S8b).

##### 1.3. Synthesis of sulfur@nitrogen-doped carbon composite (S@N-C)

A sulfur@nitrogen-doped carbon composite (S@N-C) was synthesized as the cathode active material. A nitrogen-doped carbon composite (N-C) was first synthesized via a two-step method. A mixture of 10 g nickel(II) acetate tetrahydrate ( $\text{Ni}(\text{CH}_3\text{COO})_2 \cdot 4\text{H}_2\text{O}$ , AR, Sinopharm Chemical) and 1 g urea ( $\text{CO}(\text{NH}_2)_2$ , AR, Sinopharm Chemical) was calcined at 460  $^\circ\text{C}$  for 1 h under Ar atmosphere with a ramping rate of 5  $^\circ\text{C min}^{-1}$  to get Ni@N-C. The N-C was obtained by etching the Ni in Ni@N-C with 4 M  $\text{HNO}_3$  aqueous solution (Fig. S18). Sulfur was then impregnated into the N-C by a melt infiltration method. A mixture of N-C (70 mg) and sulfur powder (210 mg, AR, Sinopharm Chemical) was sealed in a Teflon-lined stainless steel autoclave and heated at 155  $^\circ\text{C}$  for 10 h under Ar atmosphere (Fig. S19).

##### 1.4. Cathode preparation

A mixture containing 70 wt. % S@N-C, 20 wt. % conductive carbon black (Super P, TIMCAL) and 10 wt. % polyvinylidene fluoride (PVDF, Arkema) were dispersed in N-methylpyrrolidone (NMP, Aladdin Chemistry). The resulting slurry was coated on a carbon-coated Al foil (MTI) and vacuum dried overnight at 80  $^\circ\text{C}$ . The mass loading was ca. 0.91 mg  $\text{cm}^{-2}$ .

##### 1.5. Preparation of polysulfide solution

The polysulfide solution was prepared by adding 138 mg of  $\text{Li}_2\text{S}$  (99.9%, MACKLIN) and 289 mg of sulfur (AR, Sinopharm Chemical) in DME and stirring vigorously for 18 h.

##### 1.6. Electrochemical measurements

The redox potential of DiMF/Li-DiMF was measured in a three-electrode electrochemical cell. The working electrode is a Pt disk electrode ( $\phi = 3$  mm). A Pt wire electrode and a homemade Li/Li<sup>+</sup> electrode were used as the counter and reference electrode, respectively. The electrolyte is 10 mM DiMF and 1 M LiPF<sub>6</sub> in DME. The cyclic voltammogram (CV) was measured in a potential range of 0.05 V and 0.5 V (vs. Li/Li<sup>+</sup>) at the sweep rate of 5 mV s<sup>-1</sup>.

The lithiation / delithiation potentials of Al foil was measured in a three-electrode configuration. The working electrode was a single-side polished Al foil. Both the counter and reference electrodes were lithium metal foil. The separator was Celgard 2325 membrane and the electrolyte was 1 M LiTFSI in DME/DOL (1:1, v/v) with 0.4 M LiNO<sub>3</sub> additive. CV was measured in a potential range of 0.05 V and 2 V (vs. Li/Li<sup>+</sup>) at the sweep rate of 0.5 mV s<sup>-1</sup>. The electrochemical impedance spectroscopy (EIS) was measured in a three-electrode configuration using a GAMRY Reference 600+ potentiostat in a frequency range of 100k to 0.1 Hz and an amplitude of 10 mV (Fig. S15).

2032-type coin cells with Celgard 2325 separator were used for all galvanostatic charge/discharge tests. The half cells were assembled using the as-prepared anode (*c*-LiAl, *e*-LiAl, or *e*-Li/Cu) as the working electrode and a lithium metal foil (600  $\mu$ m) as the counter electrode. The symmetric cells were assembled using the as-prepared anode (*c*-LiAl, *e*-LiAl, or *e*-Li/Cu) as both the working and counter electrode. The Li-ion/S full cells were assembled using the S@N-C cathode ( $\phi = 11$  mm) and the as-prepared anode (*c*-LiAl, *e*-LiAl, or *e*-Li/Cu,  $\phi = 12$  mm). The anode / cathode areal capacity ratio was ca. 1.07:1. The electrolyte was also 1 M LiTFSI in DME/DOL (1:1, v/v) with 0.4 M LiNO<sub>3</sub> additive. All cells were tested with a LAND CT2001A battery test system.

### 1.7. Material characterization

Scanning electron microscope (SEM) and energy dispersive X-ray spectrometry (EDS) element mapping were performed on a field emission scanning electron microscope (ZEISS Merlin Compact) with an INCAPentafETx3 energy dispersive X-ray spectrometry (Oxford Instruments). Transmission electron microscope (TEM) was performed on a JEM-2100F (JEOL Compact). X-ray diffraction (XRD) was carried out using a Miniflex600 (Rigaku, 600 W, Cu K $\alpha$ ,  $\lambda = 1.5406$  Å, 2 °/min). For XRD characterization, the electrodes were sealed with Kapton tape to avoid air exposure. X-ray photoelectron spectroscopy (XPS) was performed on an ESCALAB 250Xi spectrometer (Thermo Fisher, Al K $\alpha$ ). For XPS analysis, in case of long-term exposure in ambient air, the samples were taped on a XPS sample holder in an Ar-filled glovebox, sealed in an airtight container and quickly transferred inside the XPS chamber. The power of Ar<sup>+</sup> etching was 2 kV. Raman microscopy was carried out using an XploRA PLUS (HORIBA, 638 nm Laser). Atomic force microscopy (AFM) measurement was conducted on Witec-alpha300. Thermogravimetric analysis (TGA) was carried out using a TA Q500 Instruments. Fourier Transform Infrared (FTIR) spectroscopy was carried out using a VERTEX 70 (Bruker Compact).

### 1.8. Density functional theory (DFT) calculations

The LUMO energies of PAH were calculated using the DFT/B3LYP/6-31G(d,p) methodology. The calculations of sulfur adsorption energy were performed by Vienna Ab-initio Simulation Package (VASP), using density functional theory (DFT) with a plane wave basis set and Perdew-Burke-Ernzerhof (PBE) exchange-correlation functional. The DFT-D3 method presented by Grimme was performed to describe the Dispersion interactions.

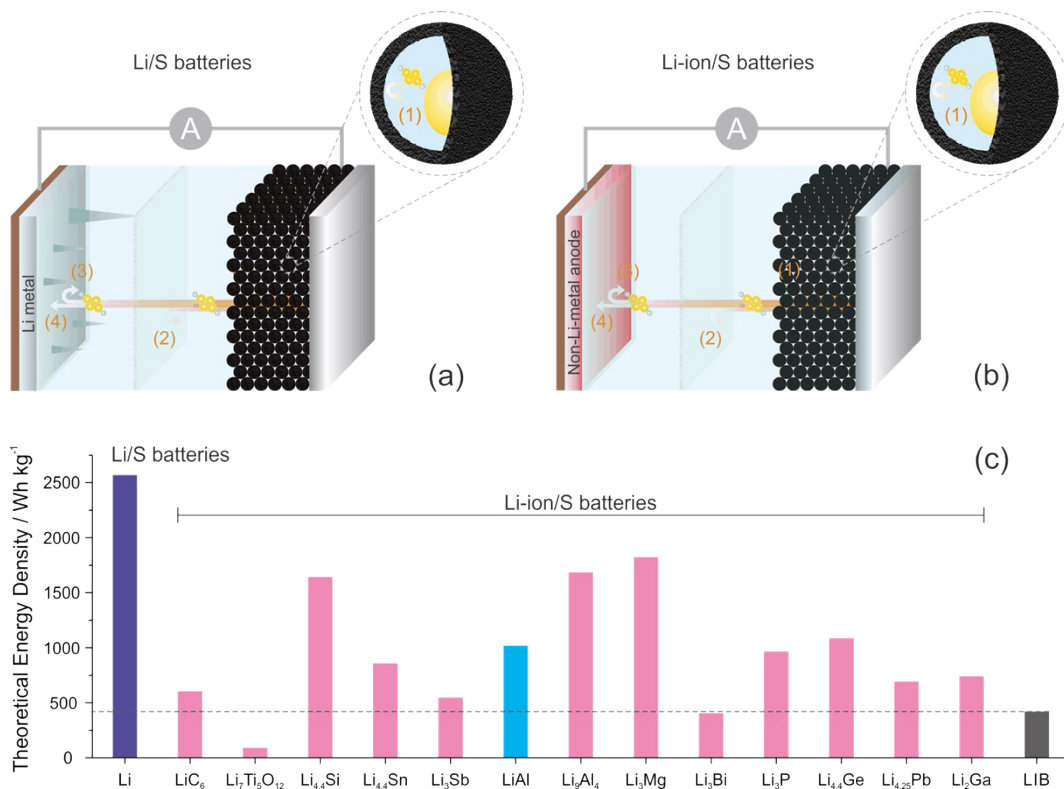


**Fig. S1.** Schematic illustration of Li/S (a) and Li-ion/S (b) batteries. Theoretical energy densities of conventional lithium ion batteries (LIB),<sup>1</sup> Li/S batteries and Li-ion/S batteries with various non-lithium metal anodes (c).

Many strategies have been adopted to address the shuttling of polysulfide intermediates in Li/S batteries, such as confining sulfur / polysulfide in porous carbon matrices (1), blocking the polysulfide crossover with functional separators (2), and preventing the contact of polysulfide and lithium metal (4) by the in-situ generated or artificial SEI layer (3). The replacement of lithium metal with non-lithium metal anodes could offer a new option to resolve the shuttling effect by selecting polysulfide tolerant anodes, which could decrease the reaction kinetics of (4). In addition, using non-lithium metal anodes could avoid the lithium dendrite formation and improve the safety. Although Li-ion/S batteries using non-lithium metal anodes have lower theoretical energy densities than Li/S batteries, they could still provide a much higher theoretical energy density than conventional LIB (c). For example, the Li-ion/S battery with LiAl anode has a high theoretical energy density of 1020 Wh kg<sup>-1</sup>, about 2.4 times of conventional LIB. Therefore, Li-ion/S batteries are promising candidates for next-generation energy storage devices.

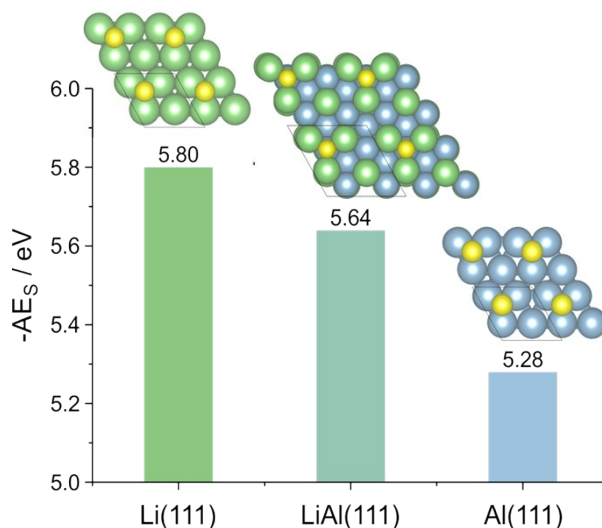


**Fig. S2.** DFT calculated sulfur adsorption energy ( $AE_s$ ) for Li(111), Al(111), and LiAl(111) surfaces.

The calculations of sulfur adsorption energy were performed by Vienna Ab-initio Simulation Package (VASP),<sup>2</sup> using density functional theory (DFT) with a plane wave basis set and Perdew-Burke-Ernzerhof (PBE) exchange-correlation functional.<sup>3</sup> The DFT-D3 method presented by Grimme was performed to describe the Dispersion interactions.<sup>4</sup> The interactions between ionic cores and electrons was described by the projector augmented wave (PAW) method.<sup>5</sup> A  $5 \times 5 \times 1$   $\Gamma$ -centered k-points grids (except for LiAl (111) surface with a  $3 \times 3 \times 1$   $\Gamma$ -centered k-points grids because of its larger lattice constant) with a truncation kinetic energy of 500 eV were used for the slab's optimization. The energy for every electron step were considered to be convergent if the change in energy was less than  $1e-5$  eV. For all optimizable atoms, the conjugate gradient algorithm was used to relax them until the force applied on them are smaller  $0.02$  eV/Å for slab. A  $c(2 \times 2)$  slab model with 4 atom layers was used during the calculations, which the top two layers were allowed to relax while the others were fixed. The vacuum layer was set to  $15$  Å along the z axis.

The  $AE_s$  for Al(111) and LiAl(111) are much lower than that for Li(111), suggesting a weaker interaction of sulfur and Al anode.

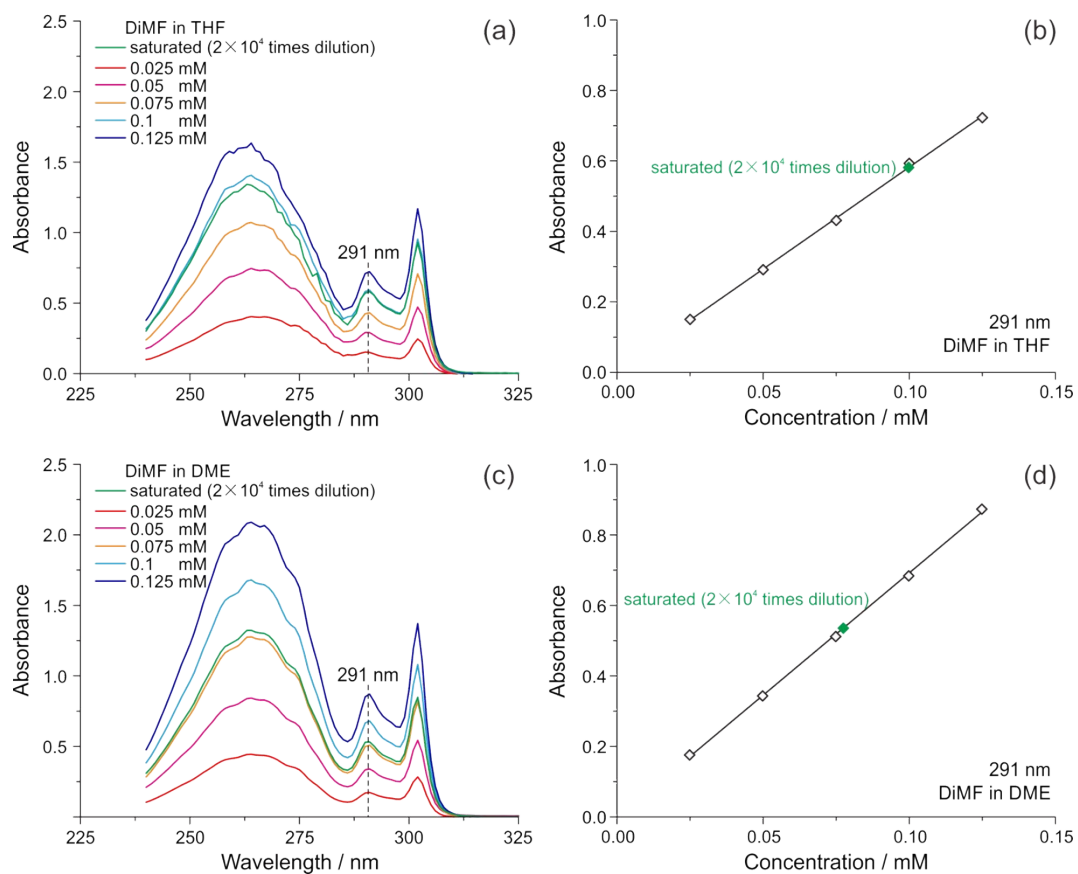


**Fig. S3.** UV-vis spectra (a, b) and calibration curve (c, d) of DiMF in THF and DME, respectively.

The solubility of DiMF are 2.0 M in THF and 1.6 M in DME. The high solubility of DiMF enables the preparation of the chemical prelithiation reagent (Li-DiMF) with a high concentration, which can accelerate the chemical prelithiation reaction.

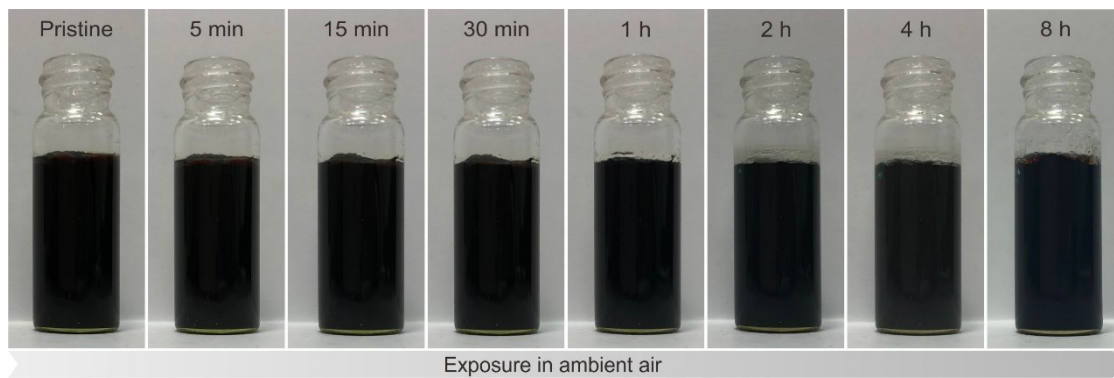


**Fig. S4.** Digital images of the chemical prelithiation reagent (1.5 M Li-DiMF/THF) exposed in ambient air for different durations. The solution exhibits a good stability in ambient air.

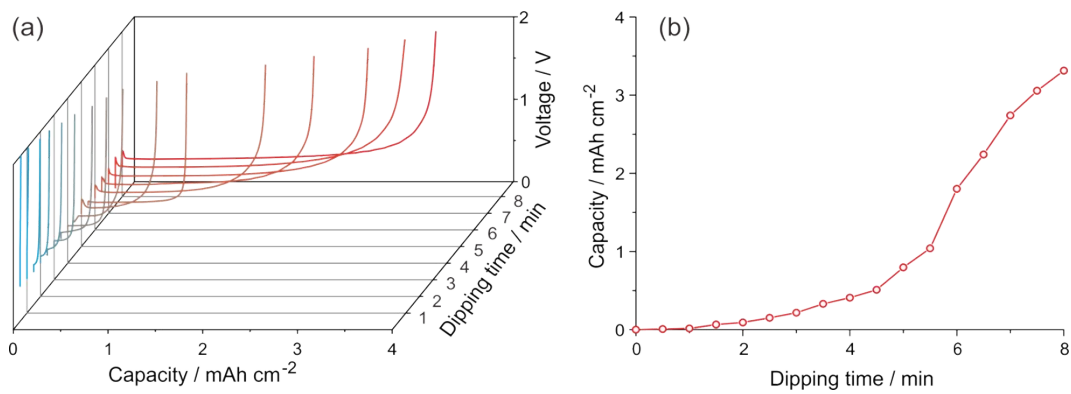


**Fig. S5.** (a) The first delithiation voltage profiles of the chemically prelithiated Al anodes (c-LiAl) with different dipping treatment duration. (b) The relation between the areal capacities and the dipping time. Obviously, the chemically prelithiated capacity, namely the amount of active Li<sup>+</sup> preloaded in Al anode, can be easily and precisely controlled by dipping time.

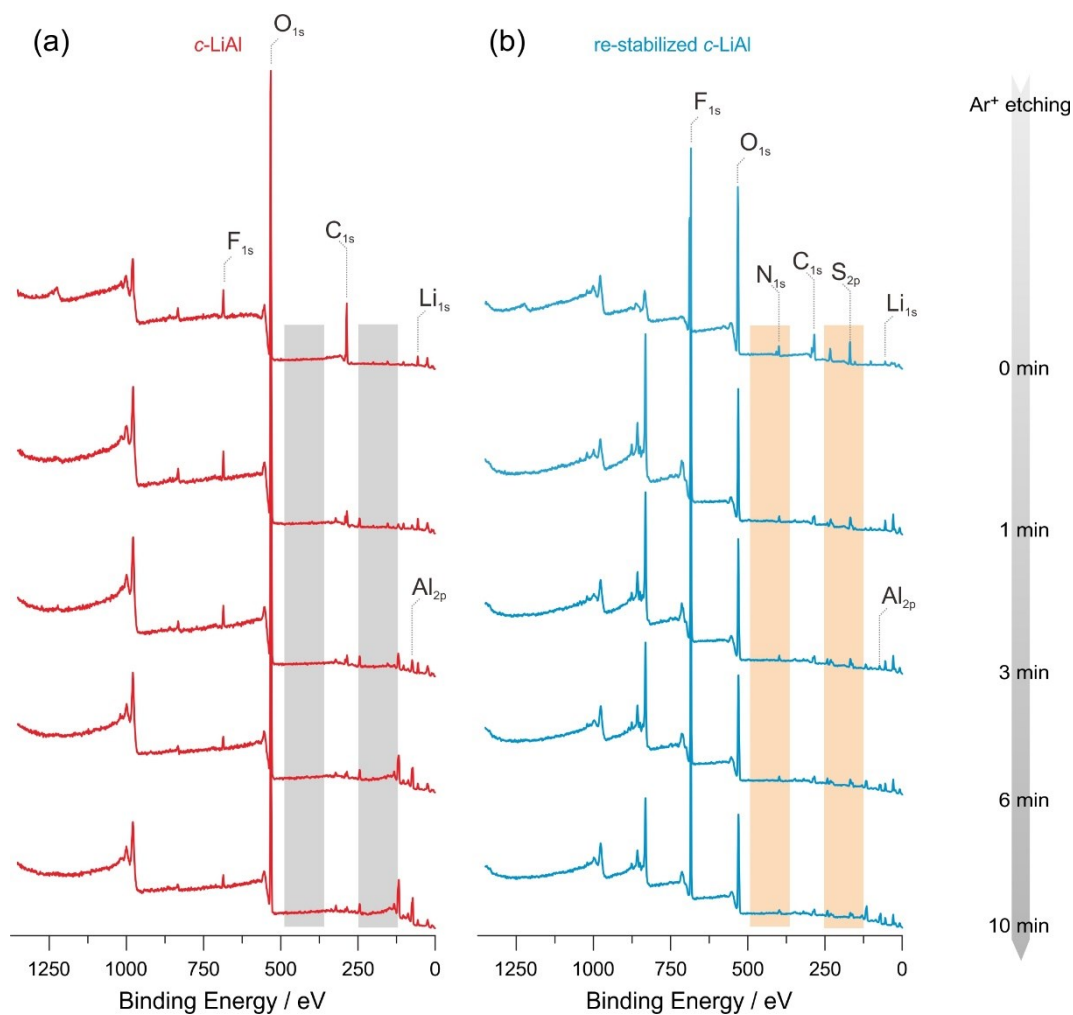


**Fig. S6.** XPS survey spectra of the c-LiAl before (a) and after (b, denoted as the re-stabilized c-LiAl) an immersion in the electrolyte of 1 M LiTFSI, 0.4 M LiNO<sub>3</sub> in DME/DOL (1:1, v/v). Apart from the O<sub>1s</sub>, C<sub>1s</sub>, and Al<sub>2p</sub> peaks, N<sub>1s</sub> and S<sub>2p</sub> peaks were detected after the immersion treatment, which indicates a reconstruction of the artificial SEI.

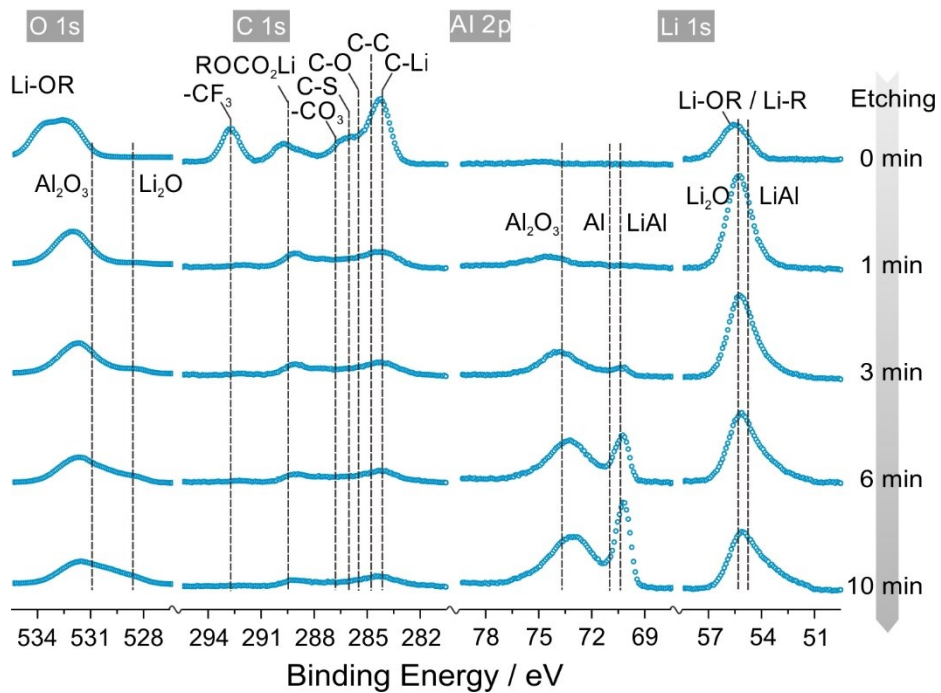


**Fig. S7.** XPS depth analysis of the re-stabilized *c*-LiAl. The possible species are shown in the figure. OR and R stand for different organic functional groups.

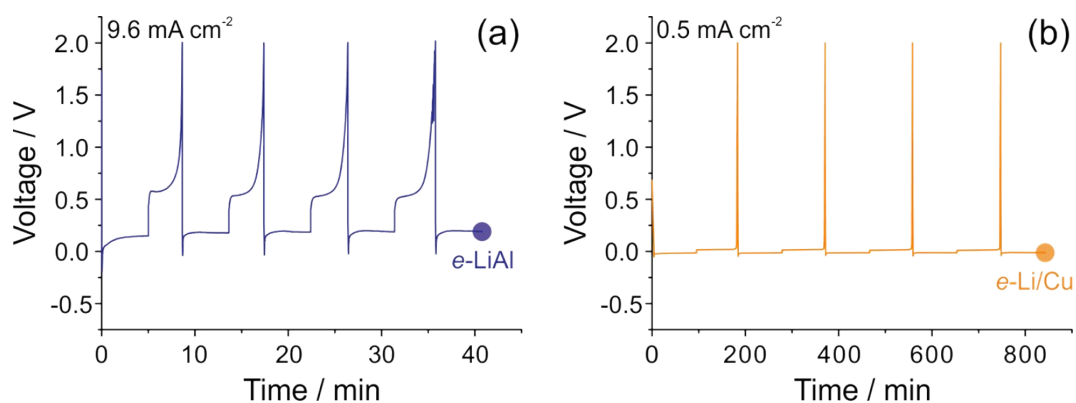


**Fig. S8.** Voltage profiles for the electrochemical preparation of *e*-LiAl (a) and *e*-Li/Cu (b).

Both *e*-LiAl and *e*-Li/Cu were obtained by five galvanostatic cycles using a half cell with lithium metal (600  $\mu\text{m}$ ) counter electrode (schematically illustrated in Fig. 3a, main text). For the preparation of *e*-LiAl, the electrochemical lithiation time of each step was 5 min and the lithiation capacity was kept 0.8 mAh cm<sup>-2</sup>, which is same as that of the *c*-LiAl prepared by 5 min chemical prelithiation. The current density was thus 9.6 mA cm<sup>-2</sup>. For the preparation of *e*-Li/Cu, the electrodeposition capacity was also 0.8 mAh cm<sup>-2</sup>. While the current density was set to be a low value of 0.5 mA cm<sup>-2</sup> in order to avoid the lithium dendrite formation.

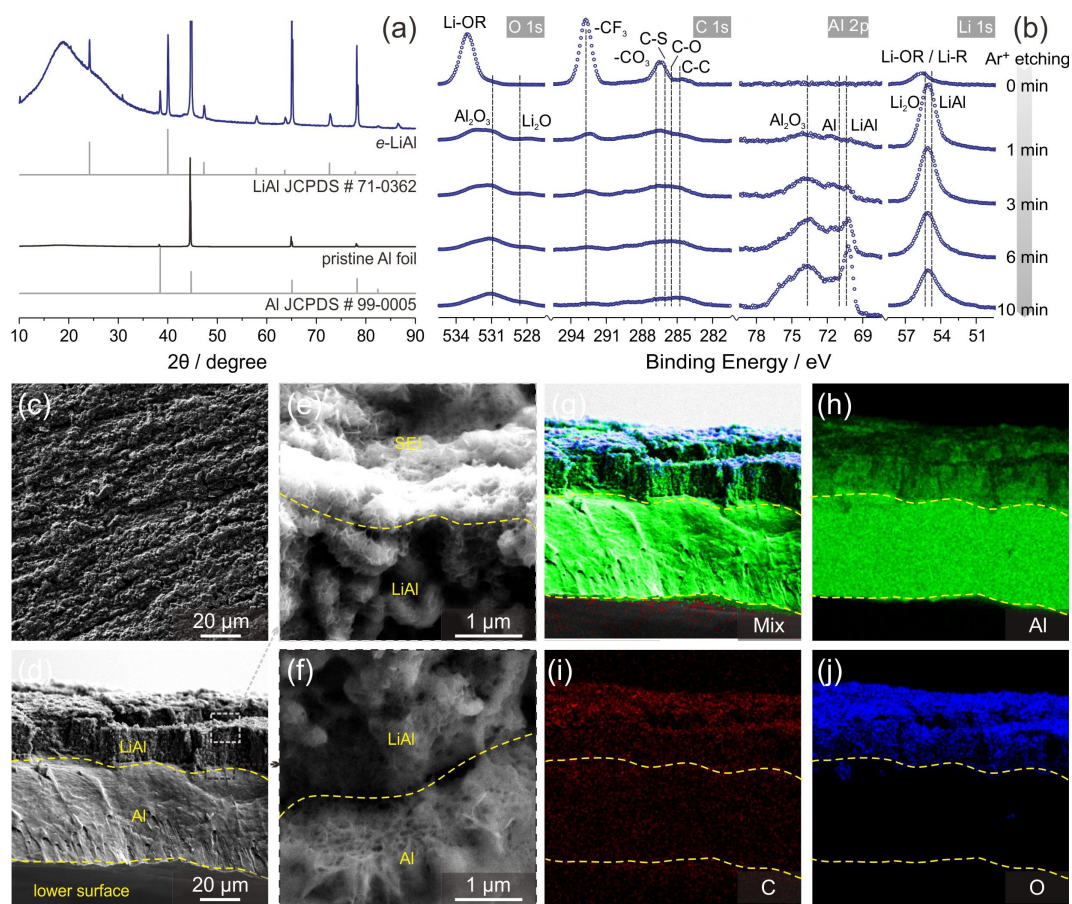


**Fig. S9.** Characterizations of *e*-LiAl. (a) XRD patterns. (b) XPS depth analysis. The possible species are shown in the figure. OR and R stand for different organic functional groups. The upper surface (c) and cross-sectional (d) SEM images. Enlarged SEM images of the upper surface (e) and interface of Al/LiAl (f) as marked by the dashed box in (d). Cross-sectional EDS element mapping (g-j).

The XRD pattern of *e*-LiAl was approximately the same as that of *c*-LiAl (Fig. 2b, main text), indicating that they have the same crystalline structure. According to the XPS analysis, the *e*-LiAl exhibited a strong C 1s peak of CF<sub>3</sub> functional groups around 292.7 eV,<sup>6-8</sup> and a weak Li 1s peak of Li-OR or Li-R around 55.5 eV at 0 min Ar<sup>+</sup> etching (Fig. S9b),<sup>9-10</sup> while the *c*-LiAl had no C 1s peak around 292.7 eV and a strong Li 1s peak of Li-OR or Li-R (Fig. 2c, main text), suggesting different SEI composition on the top surface. Both *e*-LiAl and *c*-LiAl became rough after electrochemical or chemical prelithiation (Fig. S9c and Fig. 2f in the main text). While the cross-sectional SEM images show that they have different morphologies. Compared with the densely stacked rock-like structure for *c*-LiAl (Fig. 2h and 2i, main text), the *e*-LiAl displayed a loosely aggregated structure (Fig. S9d), in which there were many nanosheets on the surface and porous structures at the LiAl/Al interface (Fig. S9e and S9f).

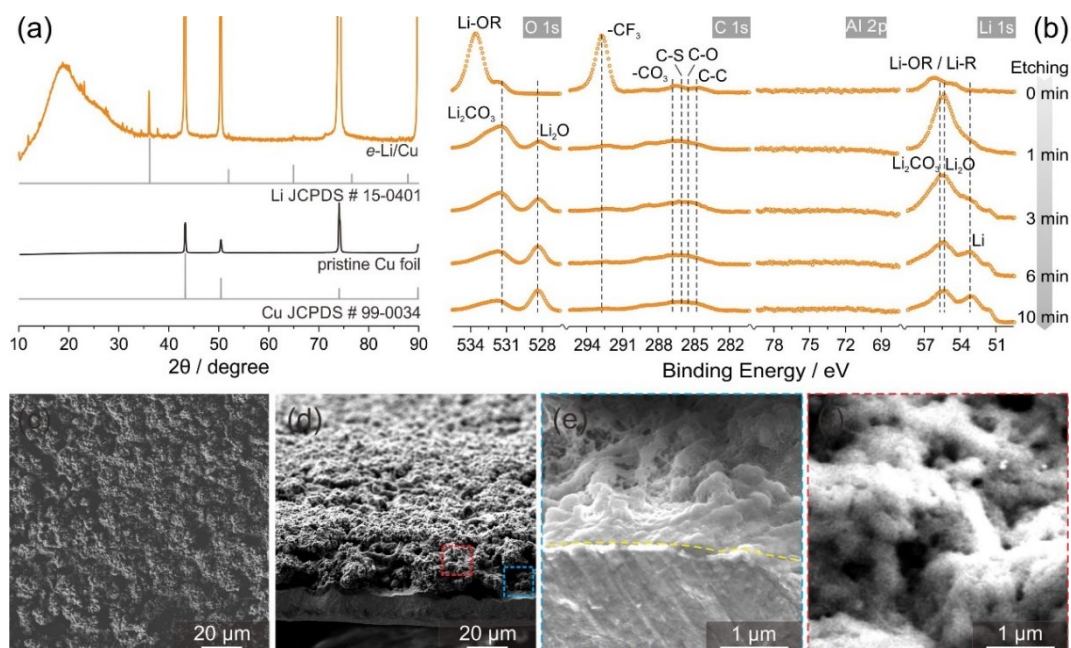


**Fig. S10.** Characterizations of *e*-Li/Cu. (a) XRD patterns. (b) XPS depth analysis. The possible species are shown in the figure. OR and R stand for different organic functional groups. Upper surface (c) and cross-sectional (d) SEM images. Enlarged SEM images of the upper surface (e) and interface of Li/Cu (f) as marked by the dashed box in (d).

Except for some diffraction peaks of the Cu foil substrate, all other diffraction peaks of the *e*-Li/Cu were well indexed to the standard pattern of Li JCPDS #15-0401. The SEI of *e*-Li/Cu contained many similar species with that of *e*-LiAl from XPS analysis (Fig. S9b and S10b). A homogeneous lithium metal layer without needle shaped dendrites was clearly observed from the SEM images.

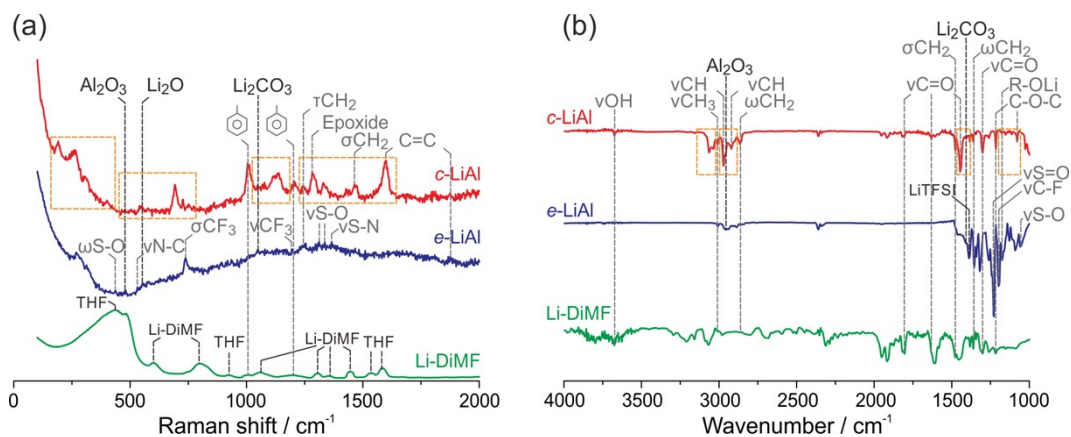


**Fig. S11.** Raman (a) and reflectance FTIR spectra (b) of *c*-LiAl, *e*-LiAl and Li-DiMF under Ar atmosphere. Characteristic peaks (black) and possible vibrations (grey) are marked in the figure.<sup>11-24</sup>

Compared with the Li-DiMF, there were some extra peaks and also obvious peak shifts for the *c*-LiAl as marked with orange dashed boxes, indicating that the artificial SEI on the *c*-LiAl surface is not the residual Li-DiMF. In addition, the *c*-LiAl exhibited many different vibrations in comparison with the *e*-LiAl, suggesting that their SEI composition are quite different.

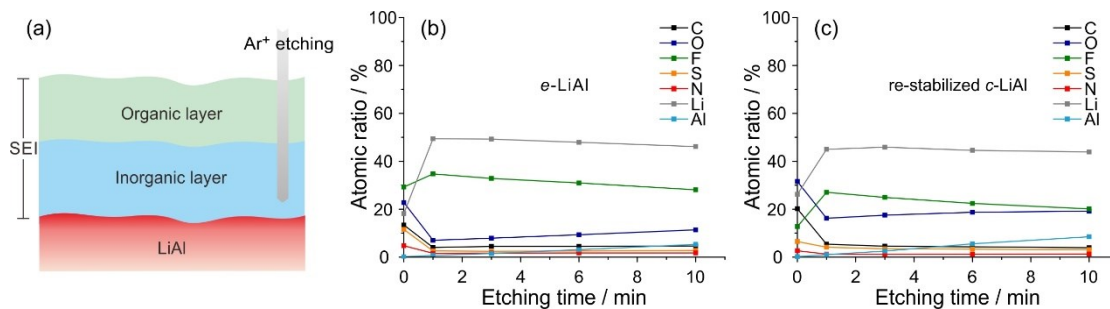


**Fig. S12.** (a) Schematic illustration of XPS depth analysis. The elemental compositions of the fresh e-LiAl (b) and the re-stabilized c-LiAl (c), obtained after an immersion treatment of the c-LiAl in the electrolyte of 1 M LiTFSI, 0.4 M LiNO<sub>3</sub> in DME/DOL (1:1, v/v) with different Ar<sup>+</sup> etching duration measured by XPS analysis.

The SEI layer is generally composed of an outer organic layer and an inner inorganic layer. The outer organic layer was removed only by 1 min Ar<sup>+</sup> etching from the notable decrease in C atomic ratio (black squares). The Al atomic ratio (cyan squares) was low even after 10 min Ar<sup>+</sup> etching. Therefore, the etching depth was still in the inorganic layer, which was mainly composed of LiF and Li<sub>2</sub>O because of the high Li (gray squares), F (green squares), and O (blue squares) atomic ratios. Given that the re-stabilized c-LiAl had a higher O atomic ratio (blue squares) relative to the e-LiAl, the re-stabilized c-LiAl may have a higher proportion of Li<sub>2</sub>O in the inner inorganic SEI layer.

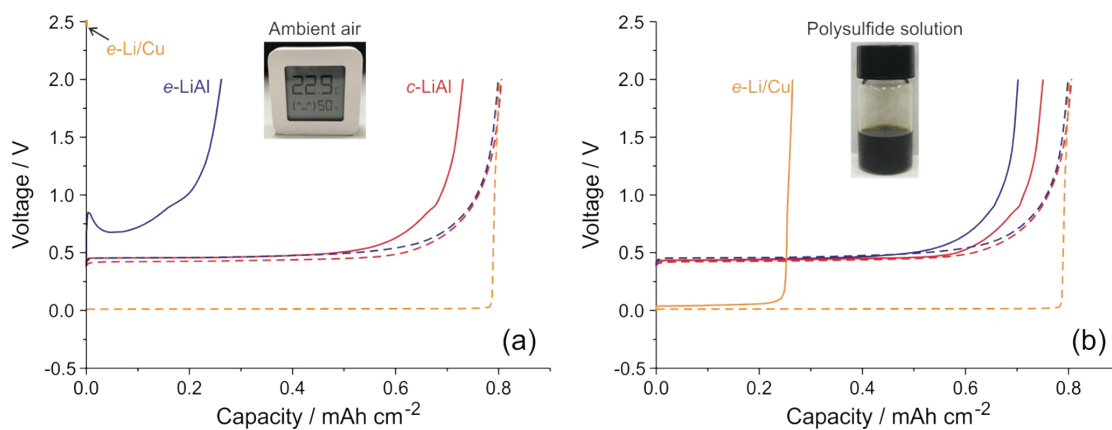


**Fig. S13.** The first delithiation profiles of c-LiAl, e-LiAl, and e-Li/Cu before (dashed lines) and after 30 min exposure in ambient air (a) or 30 min immersion in polysulfide solution (b) (solid lines). The capacity retentions are shown in Fig. 3d and 3e in the main text.

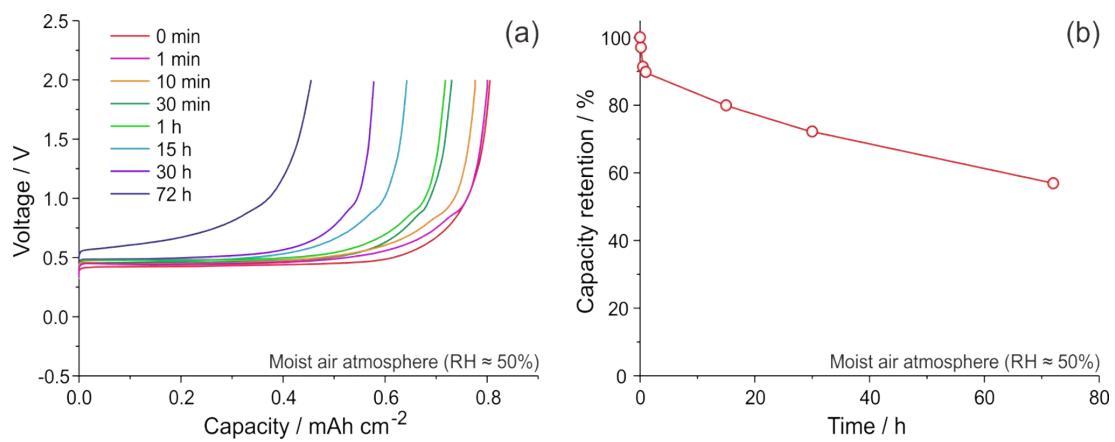


**Fig. S14.** (a) The first delithiation voltage profiles of the *c*-LiAl after exposed in ambient air with different duration. (b) The capacity retention. The *c*-LiAl exhibited an excellent stability in ambient. It still maintained a high capacity retention over 56.5% even after 72 h exposure in ambient air with a high relative humidity of 50%.

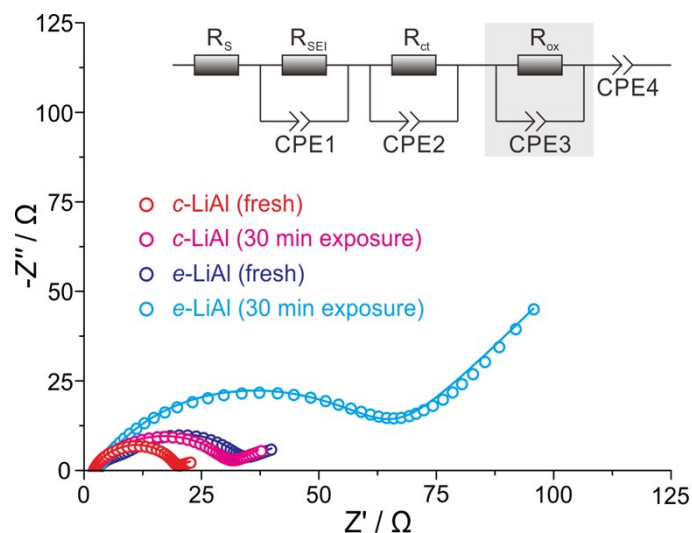


**Fig. S15.** Nyquist plots for the *c*-LiAl and *e*-LiAl before and after 30 min exposure in ambient air. Inset is the equivalent circuit used for data fitting.<sup>25</sup>  $R_s$  is ohmic resistance,  $R_{SEI}$  is SEI layer resistance,  $R_{ct}$  is charge transfer resistance,  $R_{ox}$  is an additional layer resistance induced by ambient air corrosion. CPE1, CPE2, CPE3 and CPE4 are constant phase elements.  $R_{ox}$  and CPE3 (gray box) are only used for the fitting of the *c*-LiAl and *e*-LiAl after 30 min exposure in ambient air. The fitting results are shown in Table S1.

According to the fitting results, the fresh *c*-LiAl had a smaller  $R_{SEI}$  than the fresh *e*-LiAl, which is in accordance with their different SEI as discussed above. Meanwhile, the fresh *c*-LiAl had a smaller  $R_{ct}$  than the fresh *e*-LiAl, which is probably related to their different morphologies. The fresh *c*-LiAl may have a larger electrochemical reaction interface and thus a lower  $R_{ct}$ . As shown in Fig. 3d in the main text, the *e*-LiAl was unstable in ambient air, whereas the *c*-LiAl exhibited a high resistance to ambient air corrosion. We believe that the internal structure (LiAl alloy) of *c*-LiAl remains unchanged. Both the  $R_{SEI}$  and  $R_{ct}$  for *c*-LiAl displayed negligible change and an additional process with a  $R_{ox}$  of 10.82  $\Omega$  was observed after 30 min exposure, which may be ascribed to the reconstruction of the outer artificial layer and thus the generation of a shielding layer. As *e*-LiAl lost more than 60% of its capacity after exposure in ambient air (Fig. 3d, main text), the internal LiAl alloy of *c*-LiAl was apparently reacted with oxygen, nitrogen or moisture. The SEI layer of *c*-LiAl was partly consumed and thus the  $R_{SEI}$  became lower. The large  $R_{ox}$  of 31.23  $\Omega$  may be ascribed to the generation of an oxide or nitride layer containing  $Al_2O_3$ ,  $Li_2O$ , and  $Li_3N$ , etc.

**Table S1.** EIS fitting results for the *c*-LiAl and *e*-LiAl before and after 30 min exposure in ambient air.

	<i>c</i> -LiAl (fresh)	<i>c</i> -LiAl (30min exposure)	<i>e</i> -LiAl (fresh)	<i>e</i> -LiAl (30min exposure)
$R_s$	2.03	2.20	3.22	2.94
$R_{SEI}$	1.78	1.85	3.19	1.20
CPE1-T	1.64E-05	4.43E-06	5.17E-07	2.31E-06
CPE1-P	0.95	0.98	1.09	1.06
$R_{ct}$	14.01	13.99	26.48	26.86
CPE2-T	0.00	0.00	0.00	0.00
CPE2-P	9.03E-01	8.29E-01	7.73E-01	7.76E-01
$R_{ox}$		10.82		31.23
CPE3-T		8.56E-05		3.78E-05
CPE3-P		0.81		0.78
CPE4-T	9.26E-02	4.26E-02	2.67E-02	2.98E-03
CPE4-P	0.24	0.36	0.45	0.59

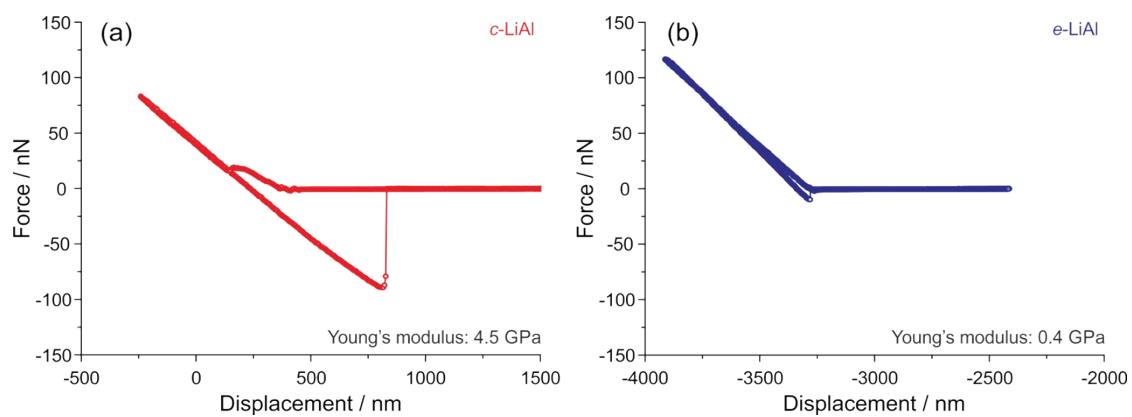


**Fig. S16.** The force-distance curves and the corresponding Young's modulus values of the *c*-LiAl (a) and *e*-LiAl (b).<sup>26</sup>

Atomic force microscopy (AFM) measurement was conducted on Wltec-alpha300. The guaranteed tip radius of curvature is < 10 nm, typically 7 nm. The artificial SEI for *c*-LiAl demonstrated a higher Young's modulus than the electrochemically is-situ generated SEI for *e*-LiAl. The improved Young's modulus may contribute to the electrode structural integrity and thus improve the cycling performance (Fig. 3b and 3c, Fig. 4b, Main text).<sup>27</sup>

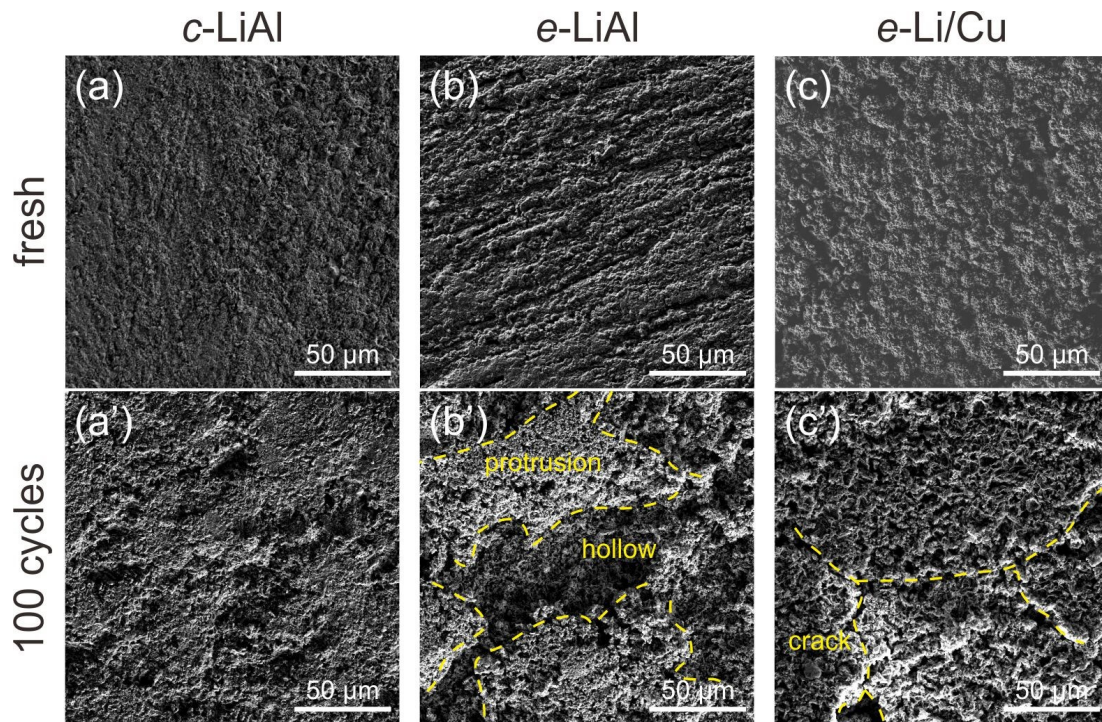


**Fig. S17.** SEM images of *c*-LiAl, *e*-LiAl, *e*-Li/Cu before (a, b, c) and after (a', b', c') 100 cycles in half cell test.

The *c*-LiAl was still integral and flat after 100 cycles, in accordance with its superior cycling performance and high coulombic efficiencies in half cell test (Fig. 3b, main text). In contrast, the *c*-LiAl became extremely uneven and the *e*-Li/Cu became cracked, corresponding to the low and unstable coulombic efficiencies, respectively.

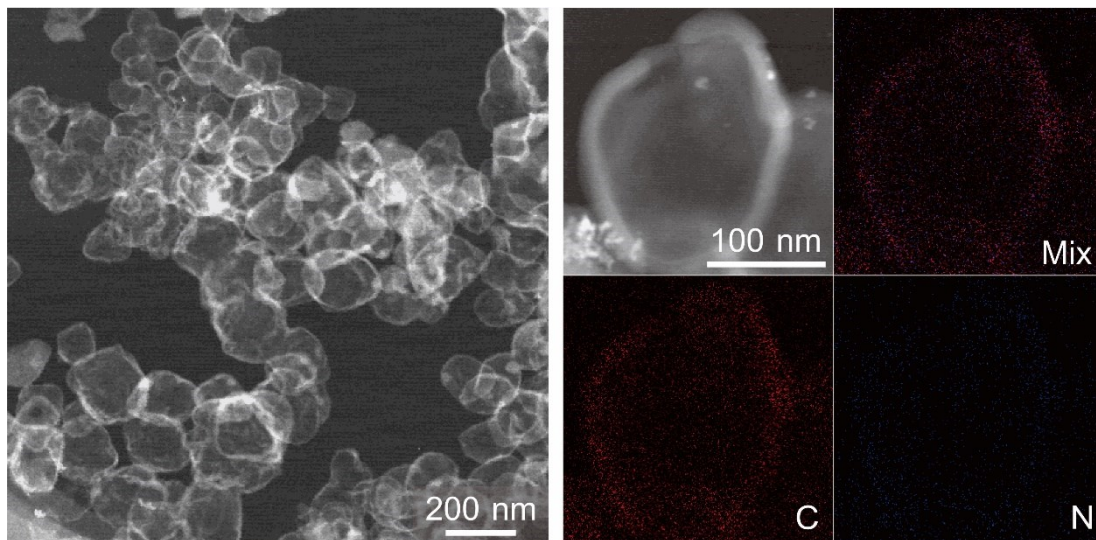


**Fig. S18.** TEM image and EDX mapping of the homemade nitrogen doped carbon (N-C). The N-C particles exhibited hollow morphology with a size around 200 nm.

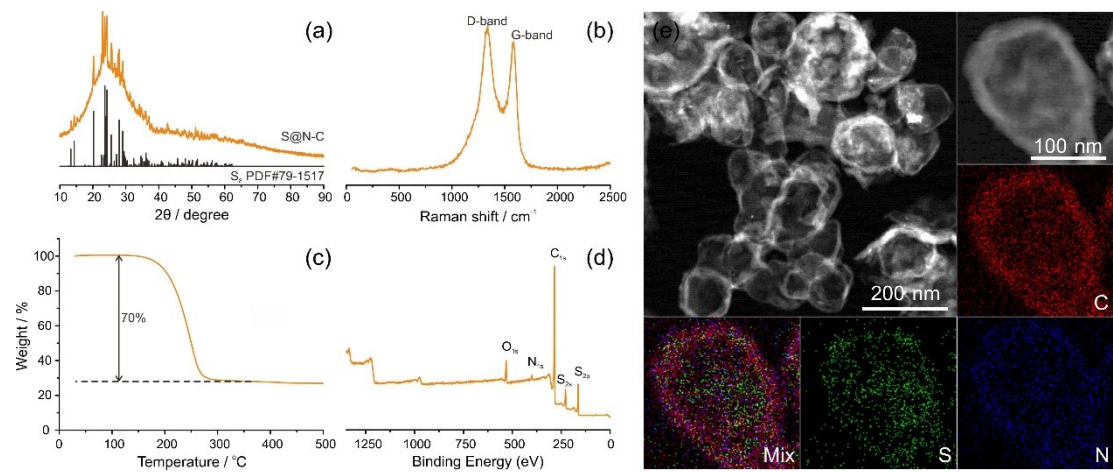


**Fig. S19.** Characterizations of the S@N-C. (a) XRD. (b) Raman spectrum. (c) Thermogravimetric analysis (TGA). (d) XPS survey spectrum. (e) TEM image and EDX elemental mapping.

The XRD pattern of S@N-C matched well with the standard pattern of S<sub>8</sub> (JCPDS # 79-1517). The D-band and G-band features corresponding to carbon were clearly observed in the Raman spectrum. The mass loading of sulfur was 70% according to TGA analysis. XPS analysis confirmed the existence of O, N, C, and S elements. From the TEM image, the S@N-C remained a similar morphology with N-C. EDX elemental mapping clearly revealed the uniform distribution of N, C, and S elements.

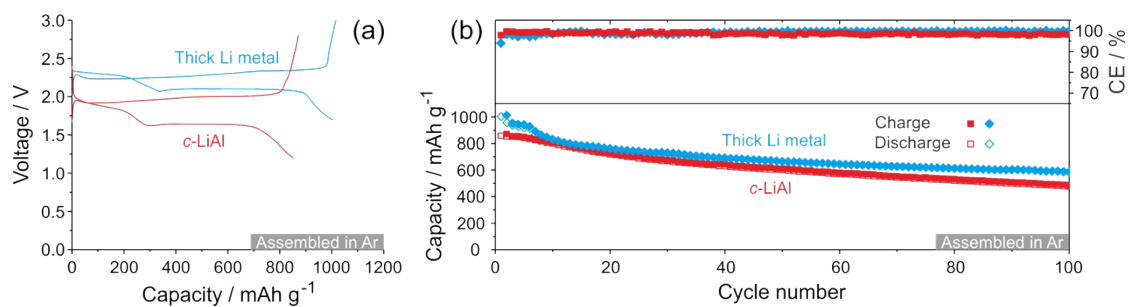


**Fig. S20.** The first cycle voltage profiles (a) and cycling performance (b) of the Li-ion/S full cell with *c*-LiAl anode and the Li/S half cell with a thick lithium metal foil (600 μm) counter electrode at a rate of 0.5 C (1 C = 1675 mA g<sup>-1</sup> of sulfur).

The Li/S half cell demonstrated a good cycling performance in 100 cycles. The cycling behavior of Li-ion/S battery with *c*-LiAl anode was close to that of Li-S half cell, suggesting that the capacity decay is mainly caused by the S@N-C cathode rather than the *c*-LiAl anode.

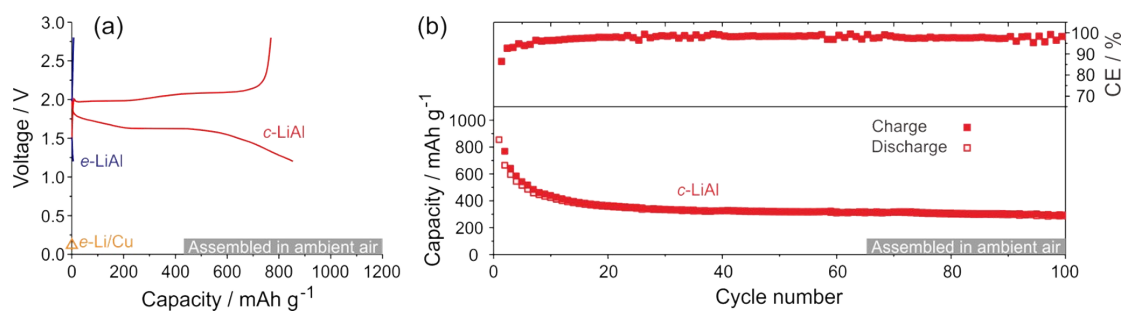


**Fig. S21.** Voltage profiles (a) and cycling performance (b) of the full cells (as schematically illustrated in Fig. 4a in the main text) assembled in ambient air at a rate of 0.5 C (1 C = 1675 mA g<sup>-1</sup> of sulfur).

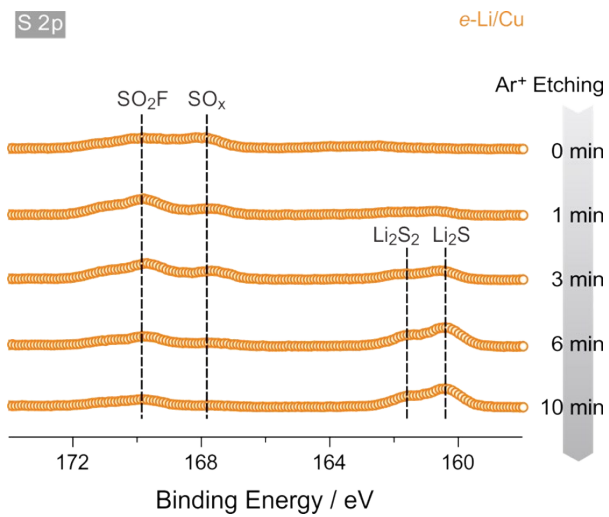


**Fig. S22.** XPS depth analysis of the c-Li/Cu after 100 cycles in Li/S full cell with the S@C-N cathode.

(a) Before prelithiation



(b) After prelithiation



**Fig. S23.** Digital images of Al foil with patterned polish before (a) and after (b) the chemical prelithiation in Li-DIMF solution. Only the polished stripe changed from silvery white to dark black, suggesting that the alumina layer on unpolished surface can prevent the chemical prelithiation of Al.

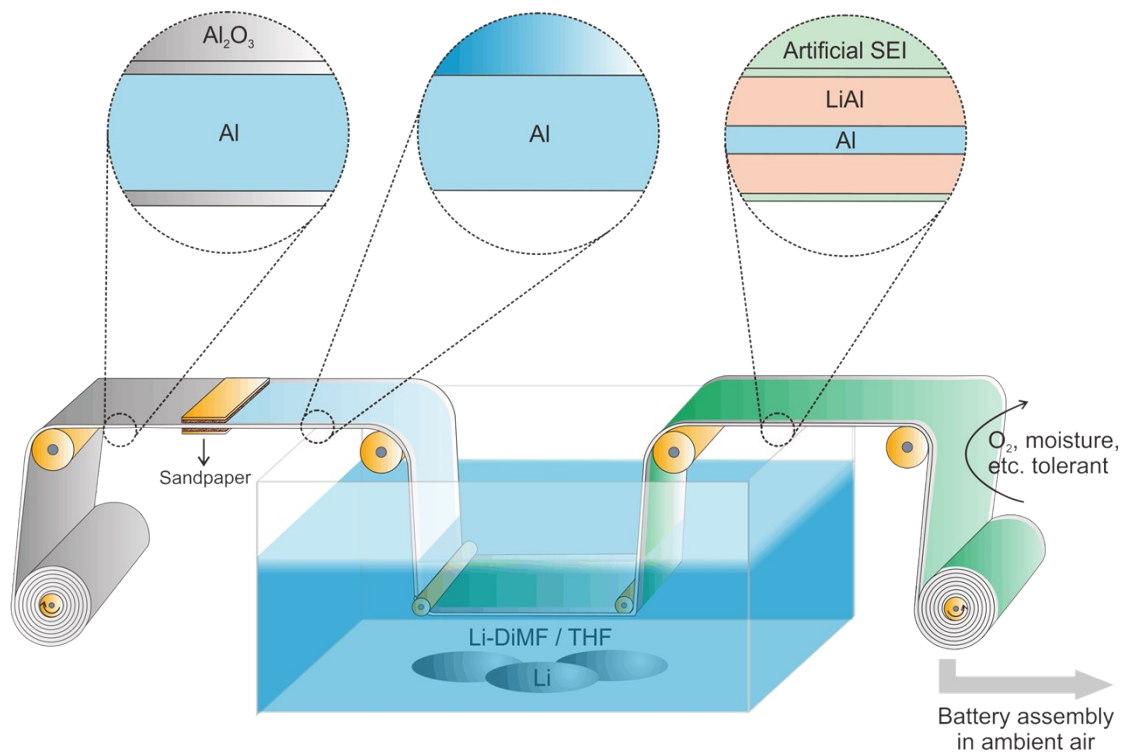


**Fig. S24.** Schematic illustration of a scalable roll-to-roll design for the preparation of c-LiAl anode.

## References

- 1 Z. W. Seh, Y. Sun, Q. Zhang and Y. Cui, *Chem. Soc. Rev.*, 2016, **45**, 5605-5634.
- 2 G. Kresse and J. Furthmüller, *Phys. Rev. B*, 1996, **54**, 11169-11186.
- 3 J. P. Perdew, K. Burke and M. Ernzerhof, *Phys. Rev. Lett.*, 1996, **77**, 3865-3868.
- 4 L. Goerigk and S. Grimme, *J. Chem. Phys.*, 2010, **132**, 184103.
- 5 P. E. Blöchl, *Phys. Rev. B*, 1994, **50**, 17953-17979.
- 6 X. Cao, X. Ren, L. Zou, M. H. Engelhard, W. Huang, H. Wang, B. E. Matthews, H. Lee and C. Niu, *Nat. Energy*, 2019, **4**, 796-805.
- 7 L. Suo, D. Oh, y. lin, Z. Zhuo, O. Borodin, T. Gao, f. wang, A. Kushima, Z. Wang and H. C. Kim, *J. Am. Chem. Soc.*, 2017, **139**, 18670-18680.
- 8 Y. Yang, D. M. Davies, Y. Yin, O. Borodin, J. Z. Lee, C. Fang, M. Olguin, Y. Zhang, E. S. Sablina and X. Wang, *Joule*, 2019, **3**, 1986-2000.
- 9 C. S. Rustomji, Y. Yang, T. K. Kim, J. Mac, Y. J. Kim, E. Caldwell, H. Chung and Y. S. Meng, *Science*, 2017, **356**, eaal4263.
- 10 L. Wang, J. Liu, S. Yuan, Y. Wang and Y. Xia, *Environ. Eng. Sci.*, 2016, **9**, 224-231.
- 11 A. K. Chan, R. Tatar, S. Feng, P. Karayaylali, J. Lopez, I. E. Stephens and Y. Shao-Horn, *J. Electrochem. Soc.*, 2019, **166**, A1867-A1874.
- 12 J. Etula, K. Lahtinen, N. Wester, A. Iyer, K. Arstila, T. Sajavaara, T. Kallio, U. Helmersson and J. Koskinen, *Adv. Funct. Mater.*, 2019, **29**, 1904306.
- 13 T. A. Galloway, L. Cabo-Fernandez, I. M. Aldous, F. Braga and L. J. Hardwick, *Faraday Discuss.*, 2017, **205**, 469-490.
- 14 F. S. Gittleson, K. P. Yao, D. G. Kwabi, S. Y. Sayed, W. H. Ryu, Y. Shao-Horn and A. D. Taylor, *ChemElectroChem*, 2015, **2**, 1446-1457.
- 15 P. C. Howlett, N. Brack, A. F. Hollenkamp, M. Forsyth and D. R. Macfarlane, *J. Electrochem. Soc.*, 2006, **153**, A595-A606.
- 16 Z. Huang, M. Zhang, J. Cheng, Y. Gong, X. Li, B. Chi, J. Pu and L. Jian, *J. Alloys Compd.*, 2015, **626**, 173-179.
- 17 M. Odziemkowski, M. Krell and D. Irish, *J. Electrochem. Soc.*, 1992, **139**, 3052-3063.
- 18 S. Suriyakumar, M. Kathiresan and A. M. Stephan, *ACS Omega*, 2019, **4**, 3894-3903.
- 19 D. Aurbach, M. Daroux, P. Faguy and E. Yeager, *J. Electrochem. Soc.*, 1988, **135**, 1863-1871.
- 20 D. Aurbach, Y. Ein-Ely and A. Zaban, *J. Electrochem. Soc.*, 1994, **141**, L1-L3.
- 21 D. Aurbach, B. Markovsky, A. Shechter, Y. Ein-Eli and H. Cohen, *J. Electrochem. Soc.*, 1996, **143**, 3809-3820.
- 22 D. Aurbach, E. Pollak, R. Elazari, G. Salitra, C. S. Kelley and J. Affinito, *J. Electrochem. Soc.*, 2009, **156**, A694-A702.
- 23 F. German, A. Hintennach, A. LaCroix, D. Thiemig, S. Oswald, F. Scheiba, M. J. Hoffmann and H. Ehrenberg, *J. Power Sources*, 2014, **264**, 100-107.
- 24 S. Y. Kim, H. T. Lee and K. B. Kim, *Phys. Chem. Chem. Phys.*, 2013, **15**, 20262-20271.
- 25 Q. Meng, G. Li, J. Yue, Q. Xu, Y. X. Yin and Y. G. Guo, *ACS Appl. Mater. Interfaces*, 2019, **11**, 32062-32068.
- 26 H. J. Butt, B. Cappella and M. Kappl, *Surf. Sci. Rep.*, 2005, **59**, 1-152.
- 27 X. Shen, R. Zhang, X. Chen, X. B. Cheng, X. Li and Q. Zhang, *Adv. Energy Mater.*, 2020, **10**, 1903645.